Journal of Colloid and Interface Science 597 (2021) 137–148

Contents lists available at ScienceDirect

Journal of Colloid and Interface Science

journal homepage: www.elsevier.com/locate/jcis

Regular Article

Direct writing of colloidal suspensions onto inclined surfaces: Optimizing dispense volume for homogeneous structures

Benedikt F. Winhard [a], Stefanie Haugg [b], Robert Blick [b], Gerold A. Schneider [a], Kaline P. Furlan [a,b,*]

[a] Hamburg University of Technology, Institute of Advanced Ceramics, Denickestraße 15, 21073 Hamburg, Germany
[b] Center for Hybrid Nanostructures, Universität Hamburg, Luruper Chaussee 149, 22607 Hamburg, Germany

GRAPHICAL ABSTRACT

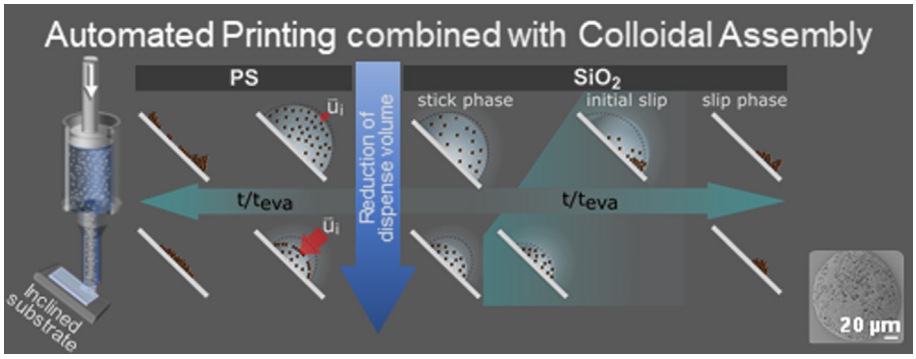

ARTICLE INFO

Article history:
Received 13 November 2020
Revised 1 March 2021
Accepted 3 March 2021
Available online 10 March 2021

Keywords:
Direct writing
Self-assembly
Inclined surface
Colloidal suspension
Photonic structure
Surface capturing effect
Confinement effect

ABSTRACT

Hypothesis: A process to fabricate structures on inclined substrates has the potential to yield novel applications for colloidal-based structures. However, for conventional techniques, besides the coffee ring effect (CRE), anisotropic particle deposition along the inclination direction (IE) is expected to occur. We hypothesize that both effects can be inhibited by reducing the dispense volume during printing by direct writing.

Experiments: We combined an additive manufacturing technique, namely direct writing, with colloidal assembly (AMCA) for an automated and localized drop-cast of polystyrene and silica suspensions onto inclined surfaces. Herein, we investigated the influence of the substrate tilting angle and the dispense volume on the printing of colloids and the resulting structures' morphology.

Findings: The results demonstrate that a reduction in the dispense volume hinders the CRE and IE for both particles' systems, even though the evaporation mode is different. For polystyrene, the droplets evaporated solely in stick-mode, enabling a "surface capturing effect", while for silica, droplets evaporated in mixed stick–slip mode and a "confinement effect" was observed, which improved uniformity of the deposition. These findings were used to generate a model of the critical droplet radius needed to print homogeneous colloidal-based structures onto inclined substrates.

1. Introduction

A printing process for fabricating large-area photonic structures on geometrically complex substrates has the potential to yield

* Corresponding author at: Institute of Advanced Ceramics, Denickestr. 15, D-21073 Hamburg, Germany.
E-mail addresses: benedikt.winhard@tuhh.de (B.F. Winhard), shaugg@physnet.uni-hamburg.de (S. Haugg), rblick@physnet.uni-hamburg.de (R. Blick), g.schneider@tuhh.de (G.A. Schneider), kaline.furlan@tuhh.de (K.P. Furlan).

https://doi.org/10.1016/j.jcis.2021.03.017
0021-9797/

Abbreviations

ALD	atomic layer deposition
AMCA	additive manufacturing combined with colloidal assembly
CRE	coffee-ring effect
CVD	chemical vapor deposition
IE	inclination effect
PhG	photonic glass
PS	polystyrene
rTBC	reflective thermal barrier coating
SD	standard deviation
SiO_2	silica
TBCs	thermal barrier coatings

Symbols

α	initial contact angle
L	capillary length
l_c	critical length for particle migration
γ	surface tension
η	dynamic viscosity
ρ	density
θ	tilting angle
c	particle concentration
c_v	saturated water vapor concentration
D	water vapor diffusivity
g	gravitational acceleration
h	droplet apex height
H	relative humidity
h_0	initial apex height
m	droplet mass
r	lateral particle position in reference to drop center
R	droplet contact line radius
R_p	particle radius
R_c	critical initial droplet radius
t	time
t_{eva}	evaporation time
t_s	time until contact line slips
u_c	height averaged capillary flow
u_i	average interface velocity at droplet apex
u_s	sedimentation velocity
u_{sn}, u_{st}	normal and tangential sedimentation velocity component, respectively
V_d	droplet volume
x_t	sedimentation distance

novel applications for self-assembled structures based on colloidal particles. For instance, thin-film organic photovoltaics are prospected to be applied on curved surfaces of various components in the future [1]. However, to date they lack the capability of absorbing the incident light due to low charge carrier mobility and a small excitation diffusion length [1]. Printing tailored photonic structures on such photovoltaics can potentially aid light harvesting by precise light management, thus enhancing their efficiency [1]. In another area related to high-temperature applications, photonic structures might pave the way to a potential new class of thermal barrier coatings (TBCs). Whereas common TBCs shield the core metal material mainly by inhibiting heat conduction, photonic coatings made out of refractory materials could additionally reflect thermal radiation, whilst providing very low thermal conductivity [2]. Working temperatures in e.g. gas turbines are continuously increasing to enhance the process efficiency. At such high temperatures, thermal radiation contributes significantly to heat transfer besides thermal conductivity [3]. Therefore, so called reflective thermal barrier coatings (rTBCs) could surpass the heat insulation properties of current TBCs due to their broadband omnidirectional reflection capabilities. To be able to withstand high-temperature exposure in the air atmosphere, they need to be produced with oxidation-resistant high-temperature stable ceramics or metals.

rTBCs can be fabricated either as a direct [4] or as an inverse photonic structure [3,5–7]. The first case comprises the three-dimensional assembly of monodisperse spherical high-temperature stable ceramic particles [8–15], while the latter comprises the co-assembly of template particles with ceramic nanoparticles [4] or infiltration of the self-assembled template with a ceramic material, which can be performed by sol–gel, chemical vapor deposition (CVD) or atomic layer deposition (ALD). For the case of template-based synthesis, the template is subsequently removed by etching or calcination, resulting in an inverse structure. ALD is especially interesting for the template infiltration, due to its capability to coat high-aspect-ratio structures, such as the 3D templates, with high precision in the sub-nm thickness range and without shadowing effect [16]. Furthermore, by applying an ALD super-cycle approach, complex atomically mixed (ternary, quaternary) ceramics can be synthesized [17].

The self-assembly of polymeric or silica particles is extensively studied and monodisperse particles of both materials are available in the market in a great variety of diameters [18]. Nonetheless, the structural arrangement and template quality, which is defined during the self-assembly process, is critical for the inverse photonic structure's properties. Thereby, controlled and tailored particle deposition and assembly is necessary to achieve high-quality photonic structures. Methods for particle assembling on planar substrates include vertical convective self-assembly [19], drop-cast [4], or spin-coating [20]. However, the aforementioned coating techniques are insufficient for complex surfaces, such as turbine blades that consist of curved parts. Note, at curved or inclined surfaces, the suspension either could drip off or get distributed unevenly.

In particular, the so-called "coffee-ring effect" (CRE) remains a major challenge for the fabrication of homogeneous films from colloidal suspensions [21]. As the name implies, it refers to the accumulation of particles at the contact line of an evaporating droplet, forming a ring-shaped stain - equivalent to spilled coffee on a plate. Deegan *et al.* [22] pioneered the research on the effect and attributed the particle deposition into such a coffee ring shape to the existence of an outward capillary flow. The flow is induced by enhanced solvent evaporation at the droplet periphery and when the contact line stays pinned during the drying process, the evaporated solvent at the droplet edge gets replaced by solvent from the center. The resulting mass transport drags suspended particles to the edge of the droplet, leading to a ring-shaped deposition. To avoid ring-shaped patterns and to print homogeneous particle deposits, the capillary flow must be avoided or compensated.

Various approaches have been investigated to suppress the CRE which can be subdivided and assigned to three different strategies [23]: contact line unpinning, manipulating the capillary flow, and hindering of particles transport to the droplet edge. In the first case, the continuously moving contact line ensures that the contact angle α remains almost constant during evaporation. Due to the

receding contact line, less or in an ideal case no evaporating solvent has to be replenished at the droplet brim, thus reducing the capillary flow [24,25]. The unpinning of the contact line can be achieved, for example, by superhydrophobic surfaces [26]. The second strategy induces additional convective flows that interfere with the outward flow [23]. Here, the most reported approach forms a Marangoni flow in the droplet that is oriented in reverse direction to the capillary flow [27]. Marangoni flow can be created by introducing a temperature or concentration gradient at the air–liquid interface of the droplet [28]. Third, inhomogeneous CRE deposition can also be mitigated by preventing the particles from migration, which is performed by tailoring the interactions between particles and the interactions between particles and interfaces, i.e. solid–liquid [29] and liquid–air interface [23]. The latter has been recently demonstrated to be promising for the fabrication of homogeneous deposits [30]. Several studies [28,30–33] revealed that particles can accumulate at the receding liquid–air interface of the droplet, forming a dense homogeneous layer, which eventually gets deposited on the substrate. This "surface capturing effect" at the droplet has been caused either by an attractive particle-interface interaction [31] or by an increased evaporation rate due to heating [32] that results in a faster droplet surface shrinkage. More details about these approaches are presented in recent reviews [23,34].

Besides the CRE, the creation of templates made from particles via 3D printing methods may also be impaired by other phenomena, especially when dealing with printing onto curved three-dimensional objects, as local inclinations may alter the particle assembly. Du *et al.* [35] presented a numerical study on drying droplets of colloidal suspensions onto inclined surfaces. Their simulation results have shown anisotropic deposition induced by the inclined surface due to depinning of the upper contact line while the lower contact line stays pinned. In a recent study by Gopu *et al.* [36] for droplets generated by electrospraying, gravity-induced deformation of the droplet shape and sedimentation was found to lead to self-assembly anisotropy, besides the different wetting time for upper and lower initial droplet region. Apart from these rather fundamental studies, colloidal self-assembly on inclined surfaces has barely been addressed in the literature to date. Yet, it is important to understand this inclination effect (IE) to develop novel printing processes for inclined and complex surfaces.

In this paper we demonstrate experimentally how the inclination of the substrate affects the self-assembly of microparticles during deposition of droplets via direct-writing. Two colloidal particle systems are investigated, namely SiO_2 and PS microparticles' water-based suspensions. Furthermore, we introduce a facile approach, to mitigate both migration effects, i.e. CRE and IE, for single droplet deposition. In a combination of experiment with theoretical calculation, we illustrate how the reduction of the initial droplet volume directly affects the particle migration on horizontal as well as tilted planar surfaces. Our results provide an optimum parameter space regarding droplet size and colloidal deposition quality.

2. Experimental section

2.1. AMCA process

Aqueous-based monodisperse silica and polystyrene suspensions with particle diameters of 2.96 μm for SiO_2 (SD = 0.07 μm) and 3.20 μm for PS (SD = 0.13 μm, Microparticles GmbH), and particle concentration of 10 mg/mL were deposited on non-tilted and tilted aluminum oxide substrates (0.53 mm thick sheets cut along A-plane, Crystec GmbH). To incline the aluminum oxide surface with a certain angle, a custom-made stage printed by fused deposition modeling was used. The room temperature and relative humidity were tracked during measurements and varied slightly from 21 to 22 °C and 19 to 27%. Syringes with a 25 μL barrel volume (1702 RN, Hamilton Company) were filled with the colloidal suspensions (Particle concentration: 10 mg/mL) prior to the direct writing process.

For the droplet formation, stainless steel needles with 51 and 151 μm of inner- and outer diameter, respectively, (34 Ga, 51 μm of internal diameter, 9.53 mm length, point style 3 from Hamilton Company) were used as they gave the highest printing resolution in previous trials. To position the substrate below the needle tip, but also to regulate the dispense volume for a single droplet, four linear stages were utilized (M−126.2S1, Physics Instruments). To drive all stages for the drop deposition, macros were written with GCS command set (Mercury™ GCS Commands, Physics Instruments) and executed with the supplied software.

For the deposition the following steps were performed successively: after positioning the substrate and needle, a pendant drop with defined volume was formed at the needle tip. The substrate approached the needle tip vertically (in the opposite direction of gravitational force) until the pendant droplet touched the surface. By retracting the substrate, the droplet remained pinned on the surface, however, detached from the needle tip. This was performed to avoid droplet 'splash' and maintain a direct writing approach, rather than an inkjet printing approach. For each parameter set, a minimum number of 10 repetitions were conducted.

2.2. Characterization

The printing process was monitored and recorded by a CMOS camera with a 5x optical magnification lens (EO-10012C ½" CMOS, Edmund Optics) mounted next to the sample stage, enabling the droplet evaporation monitoring in cross sectional view. Single evaporating droplets were recorded for each condition. The average shrinkage velocity u_i was assessed subsequently at the drop apex with the footage using an in-house custom MATLAB (Mathworks, Natick, MA) script. The dried depositions were analyzed with a light microscope (Olympus) as a first analysis after the printing process. Especially for deposits with multiple particle layers, light microscopy was not sufficient to assess the homogeneity of the deposit. Here, height profiles were additionally attained with the DektakXT profilometer by Bruker. The profiles were obtained by using a stylus with a radius of 2 μm (B-Type) and the following measurement parameters were applied: standard scan type, scan range of 65.5 μm, profile type "Hills & Valleys" and a stylus force of 1 mg. Scan length and duration were adjusted accordingly to attain a scan resolution of about 0.2 μm/pt. For the 4.2 nL SiO_2 deposition an optical profilometer (Alicona G4 Infinite Focus) was used with a 50x optical magnification lens resulting in a scan resolution of < 0.2 μm/pt, because the previous contact profilometer would have damaged the sample. Insights in the self-assembled photonic structure were obtained by SEM imaging (Zeiss Supra VP55) using low voltage of 1.5 kV and working distance of around 5 mm.

3. Results and discussion

3.1. Colloidal self-assembly on inclined surfaces: Effects and resulting structures

In the first round of experiments, single droplets of both particle suspensions were printed on aluminum oxide surfaces with an initial volume of 208.7 nL and were dried at room temperature. The substrate surfaces were either horizontally flat or inclined with a

tilting angle of 23 or 45°. On horizontally aligned surfaces, droplets of both PS (Particle radius: 1.6 μm) and SiO_2 suspensions (Particle radius: 1.48 μm) formed either a usual coffee-ring or a non-homogeneous deposit with a height-dip, respectively, as it can be observed from the SEM images and the profilometer measurements (Fig. 1a, d). Whereas PS-particles formed a disc shaped deposit of about 1 mm in diameter and about 11 μm in height, the SiO_2 microparticles assembled in a smaller but higher deposit (0.36 mm and 59 μm respectively). This coincides with the observed evaporation mode of each suspension: droplets of the PS suspension dried with a constant contact line radius (stick mode), which indicates a self-pinning effect caused by PS particles at the contact line [37,38]. Droplets containing SiO_2 particles, however, evaporated in an intermediate "stick–slip" mode, i.e. pinned contact line at the beginning of the evaporation but sudden slip initiates the "slip mode" phase with a continuously receding contact line until the solvent is fully evaporated. In the second phase of the evaporation, i.e. the slip-mode, the receding contact line apparently constricts SiO_2 particles. As a consequence, silica particles assemble in a dome-shaped deposition. The initial contact angle is very similar for both suspensions, accounting for 84° and 87° for PS and SiO_2 respectively, excluding superhydrophobicity as a possible reason for a dome-shaped assembly.

The inclination of the substrate affected the deposition and assembly of both microparticle-suspensions. For all conditions, the bottom part of the SEM images is equivalent to the lower contact line (downslope) of the drying droplet on the surface, whilst the red arrow indicates the previous alignment of droplet on the tilted surface and measured height profile position. At 23° incline, the PS deposition does not significantly differ from the previous deposition on the horizontally aligned surface (Fig. 1b). A coffee-ring was formed, but particles in the center spread homogenously. Increasing the inclination up to 45°, however, entirely altered the colloidal assembly process (Fig. 1c). A brighter area in the upper half of the SEM image indicates exposed substrate areas with overall less particles than in the lower half of the PS deposition. The corresponding profilometer measurement along the red arrow in Fig. 1(c) confirms a lower particle density and lower thickness in the upper half. The coffee-ring remains but possesses a higher thickness at the bottom than at the top. A similar IE occurs already at 23° incline for silica deposits with the concomitant formation of a small coffee-ring (Fig. 1e). Here, the overall deposition shape was altered, shifting from a circular dome-shape to a "kidney"-shape. The IE becomes even more dominant for 45° incline (Fig. 1f). Similar to the PS particle assembly, the deposition height profile is non-uniform, being thicker at the bottom than at the top.

In a previous study, Du *et al.* [35] investigated the effect of surface inclination on coffee-ring formation. In agreement with our results, their results also showed a higher particle concentration downslope than upslope. The anisotropic deposition was ascribed to the stick–slip evaporation of the droplets. Upon reaching a critical contact angle, the upper contact line slipped. i.e. stick–slip mixed evaporation mode or dynamic contact line. A thin deposition remained at the initial contact line position upslope, while particles at the lower contact line continued to assemble [35]. However, in this study droplets of PS suspension stayed pinned during the entire evaporation time (See Supplementary Information, Fig. 1). Therefore, the IE for PS suspensions cannot be explained by just contact line-slip events.

A non-uniform droplet shape generated due to gravitational deformation may also impair colloidal self-assembly on inclined surfaces [36]. This occurs either by alteration of the capillary flow that transports particles to the droplet periphery or by the downslope shift of the droplet apex, which may entail more particles to deposit downslope as there is more colloidal suspension present there than in the upslope region. As the initial contact radii of the

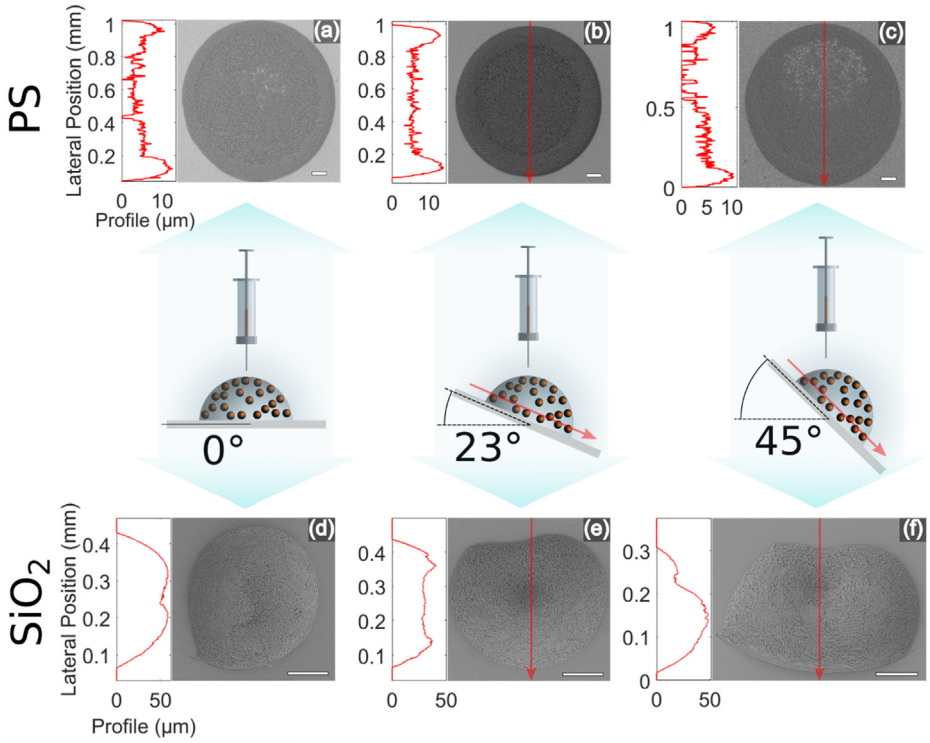

Fig. 1. Self-assembled structures fabricated with 208.7 nL initial droplet volume of (a, b, c) PS and (d, e, f) SiO_2 suspensions at different inclination angles from 0° (flat) up to 45°. SEM images show the resulting particle depositions for each parameter set. The scale bars represent 100 μm for PS and 20 μm for SiO_2. The red arrows in the schemes as well as in the SEM images show the direction of inclination as well as lateral position of the height profiles. (For interpretation of the references to colour in this figure legend, the reader is referred to the web version of this article.)

sessile droplets in our experiments were about 0.5 mm, all droplet dimensions were smaller than the capillary length $L = \sqrt{\gamma/\rho g}$ for water (L = 2.7 mm), where γ is the surface tension, ρ is the density of the liquid and g the gravitational acceleration [39]. Therefore, gravity did not significantly affect the droplet shape (see videos in Supplementary Information), which consequently did not affect the particle assembly on inclined surfaces. In this study, all droplets were considered as spherical caps.

Even though gravity did not induce a significant deformation of the droplet shape, it may have triggered the IE. A primary velocity component for microparticles in fluid is their sedimentation velocity u_s induced by gravity (Fig. 2a). Stokes' law describes this sedimentation velocity by [28]:

$$u_s = \frac{2R_P{}^2 \Delta\rho g}{9\eta} \quad (1)$$

Here, R_P is the particle radius, $\Delta\rho$ the density difference between particle and surrounding phase and η the dynamic viscosity. For a tilting angle $\Theta > 0$ the sedimentation velocity vector $\vec{u_s}$ can be subdivided in its normal and tangential component $u_{sn} = \cos(\theta)u_s$ and $u_{st} = \sin(\theta)u_s$, respectively (with regards to the printing surface, Fig. 2a). The tangential component u_t extracts the travelling velocity along the printing surface. A maximum distance that was solely been travelled due to sedimentation thus can be computed by $x_t = \sin(\theta)u_s \cdot t_{eva}$, where t_{eva} is the measured total evaporation time.

A single PS microparticle would therefore drift up to 0.04 mm at 45° surface incline during droplet evaporation (Fig. 2b). With a density of 1.05 g/cm^3, PS microparticles possess just a slightly higher density than their surrounding liquid, leading to slow sedimentation velocities and small drifts. In contrast, a maximum travel distance of 0.33 mm and 0.60 mm could be achieved by silica particles ($\rho_{silica} = 1.85 \frac{g}{cm^3}$) for 23° and 45° incline. The latter distance is bigger than the initial average droplet radius of 0.5 mm for the deposits produced with 208.7 nL. The red and blue dashed circular lines in Fig. 2 (c) represent the outline and position of the initial contact line in regards to the corresponding final particle deposits. Whereas PS particles distributed over the entire wetting area, SiO_2 assembled solely at the lower contact line. The relative changes of the calculated sedimentation induced distance x_t for a single particle in dependence of both, the surface inclination as well as particle type, are in good agreement with the observed particle depositions. Therefore, sedimentation of particles induced by gravity is considered as the primary reason for the IE in PS droplets and a combination of gravity-induced anisotropy and dynamic contact line (later discussed) for SiO_2 particles.

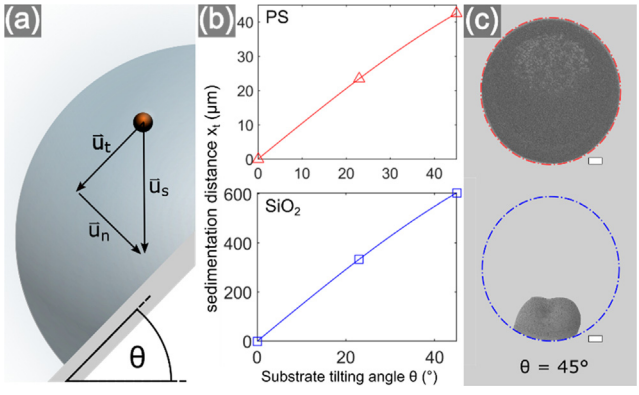

Fig. 2. (a) Schematic drawing showing the sedimentation velocity vector $\vec{u_s}$ as well as its resolving tangential and normal components ($\vec{u_t}$, $\vec{u_n}$ respectively) for a single particle in a droplet. Here, Θ represents the substrate tilting angle and x_t, the sedimentation distance parallel to the substrate, shown in (b), varies significantly depending on the particle type and substrate inclination. (c) SEM images of particle deposits for a substrate inclination of Θ = 45° and an initial droplet volume of 208.7 nL (upper: PS particles; lower: SiO_2 particles). The dash dot lines mark the initial contact line position of the deposited droplets. The scale bars represent 100 µm.

Both CRE and IE inhibit homogeneous colloidal self-assembly on inclined surfaces. The two effects are, however, based on different mechanisms. The coffee ring forms due to outward capillary flow that transports particles to the contact line, whereas gravitational sedimentation induces tangential drift. An approach to compensate both deposition effects for PS and SiO_2 microparticles must therefore be highly versatile in application, such as the dispense volume control during 3D printing.

3.2. Influence of the dispense volume

To assess the influence of the dispense volume, the substrate inclination angle was kept fixed at 45° and the initial droplet volume was varied from 4.2 nL to 208.7 nL (Fig. 3). PS deposits for an initial droplet volume of 41.7 nL and 20.9 nL (Fig. 3b, c) look similar to the previous 208.7 nL deposition (Fig. 3a) and both effects, namely CRE and IE, are observed. The particle assembly for an initial droplet volume of 4.2 nL, however, neither shows a ring-shaped particle accumulation nor an anisotropic particle distribution along the inclination direction (Fig. 3d). For silica suspensions, the shape of the entire deposition becomes more elliptical, when reducing the droplet volume to 41.7 nL (Fig. 3f). The cross-sectional profile of the deposition remains asymmetric, though. At 20.9 nL the silica particles form a flat dome. The colloidal self-assembly shows no IE (Fig. 3g). For even smaller volume (4.2 nL) an almost symmetrical dome shaped deposit is formed (Fig. 3h). For this deposition a cross sectional profile was acquired using an optical profilometer, as the contact profilometer would damage the sample during measurements. Reducing the initial droplet volume, therefore, not only increases printing resolution but also shows to be a versatile approach for reducing the coffee ring and IE.

Furthermore, the particles assembled either in an ordered or disordered structure depending on the particle type. Representative SEM images for both, PS and SiO_2 particles, are shown in Fig. 3i, k. Here, deposits of droplets with the smallest initial droplet volume are illustrated exemplarily, as the resulting depositions possess the highest uniformity.

PS particles assembled without order; thus, the assembly can be categorized as photonic glass (PhG). Printed over an entire area, these PS microparticle deposits could possibly be used as templates for inverse PhG, which are favorable for rTBC applications. The SiO_2 particles, however, mainly formed ordered assemblies (Fig. 3k). Due to the overall dome shape of the deposits, the particles formed multiple ordered grains that are separated by smaller disordered regions (Fig. 3h). Here, it should be highlighted that the SiO_2 microparticles, with 2.96 µm in diameter, assembled in an ordered structure. This is different from what was observed in previous studies [40], in which the assembly of large particles with high density (>2 $\frac{g}{cm^3}$) have been stated to be quite challenging, with the need for development of a special assembly process based on isothermal heating evaporation induced self-assembly [40]. The majority of previous studies were based, however, on conventional deposition methods such as vertical convective self-assembly or spin coating, where sedimentation and drift induced by centrifugal forces play a major role. The possibility to obtain ordered deposits for high-density particles may be seen as an advantage of the current proposed method, additive manufacturing combined with colloidal assembly. Nevertheless, it is important to mention that the SiO_2 structure could have formed an ordered structure only at the first layers visible in the SEM, as the interaction between par-

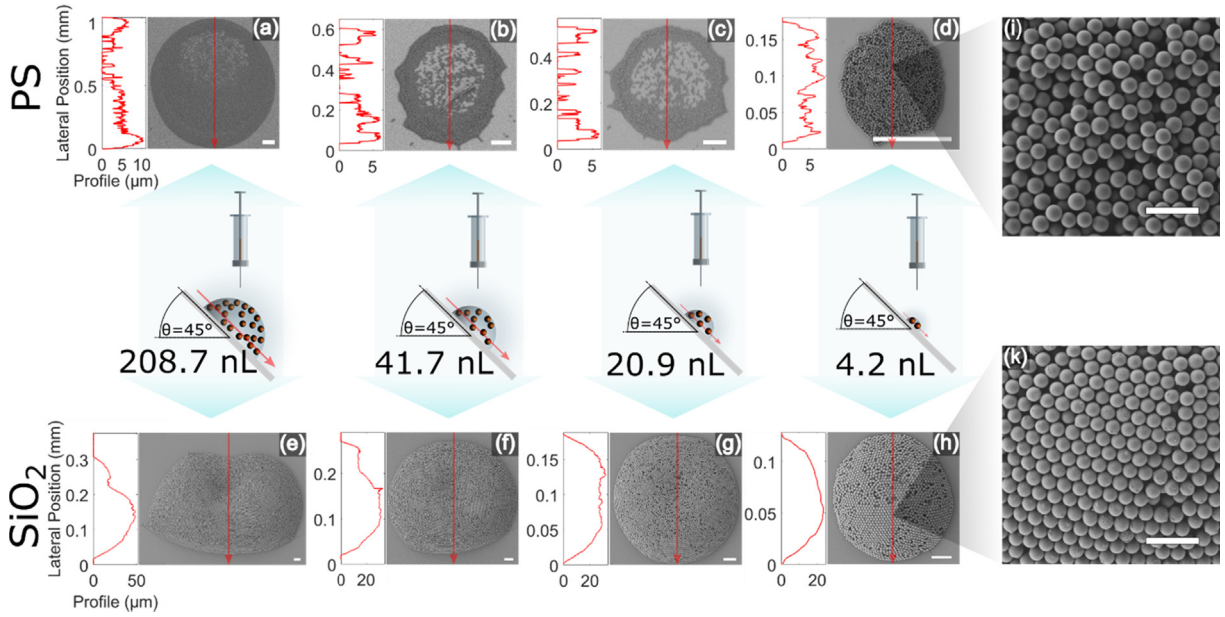

Fig. 3. Self-assembled structures fabricated with different initial droplet volume (4.2, 20.9, 41.7 and 208.7 nL) deposited on a substrate with a 45° inclination: (a, b, c, d) PS particles and (e, f, g, h) SiO_2 particles. SEM images show the final particle depositions for each parameter set indicated in the center of the image. The scale bars for PS deposits represent 100 μm for PS and 20 μm for SiO_2. The red arrows show the direction of inclination (arrows are directed downward) as well as lateral position of the height profiles. (i) and (k) show representative particle assemblies for the PS and SiO_2 suspension (a full version is available at Figure S2). Scale bar = 10 μm. (For interpretation of the references to colour in this figure legend, the reader is referred to the web version of this article.)

ticles of the same charge, i.e. particles still in suspension and particles already deposited, is repulsive and thereby promotes ordering. Moreover, the fact that SiO_2 suspensions (high-density) formed ordered deposits, whilst PS suspensions (low-density particles) formed photonic glasses (disordered) structures was surprising. As discussed before, sedimentation is much more significant for SiO_2 particles than PS particles and thereby, the lack of ordering cannot be explained solely by the sedimentation. Furthermore, both particle types and the aluminum oxide substrate possess a negative surface charge under the experiments' conditions. Hence, both particles suffer repulsion by the substrate. The difference of the deposits may be explained by the different contact line behavior, i.e. whether the suspension evaporated in stick, pinned contact line, or slip-mode, dynamic contact line. Whereas PS suspension evaporated with a pinned contact line, the SiO_2 particles were able to drift along the substrate surface due to the moving contact line (Fig. 2c and Supplementary Information videos SV1 and SV2). These differences are highlighted in the following section.

3.3. Influence of the particles' material

3.3.1. Polystyrene suspension

Several aspects must be considered when analyzing particles' self-assembly, including, but not restricted to, interface velocity, capillary flow, sedimentation and diffusive transport. In the following, we describe the velocities relevant to explain the coffee ring and inclination effect observed in this work. The evaporation of the sessile droplets was filmed in cross sectional view and the droplet height, i.e. the minimum distance between apex and surface, was tracked for different initial droplet volumes of the PS-suspension (See Figure S3 and videos SV1, SV2). An overlay of exemplary drop apex evolutions for each considered droplet volume indicates longer evaporation times for bigger droplets and vice versa. However, the apex decline rate, i.e. the slope of the droplet height evolution, is greater for smaller droplet volumes. Therefore, the average droplet surface shrinkage gets accelerated by reducing the initial droplet volume [32,36]. Such acceleration can also be promoted by an increase in the substrate temperature, as demonstrated by Li *et al.* [32].

The data points obtained in this work fit very well to the analytical solution derived by us for the apex height decline $h(t, R, \alpha)$ as a function of the time t, the pinned droplet radius R, and the contact angle α (for the detailed calculation steps please refer to the expanded section in the Supplementary Information)

$$h(t,R,\alpha)=\frac{-2\,2^{1/3}R^2+2^{2/3}\left(h_0(R,\alpha)^3+3h_0(R,\alpha)R^2+3\beta(\alpha)Rt+\sqrt{4R^6+\left(h_0(R,\alpha)^3+3h_0(R,\alpha)R^2+3\beta(\alpha)Rt\right)^2}\right)^{\frac{2}{3}}}{2\left(h_0(R,\alpha)^3+3h_0(R,\alpha)R^2+3\beta(R,\alpha)Rt+\sqrt{4R^6+\left(h_0(R,\alpha)^3+3h_0(R,\alpha)R^2+3\beta(\alpha)Rt\right)^2}\right)^{\frac{1}{3}}} \tag{2}$$

which is based on the previous analytical solution proposed by Hu and Larson [27] for the time dependent mass loss of a pinned sessile droplet: $-\dot{m}(t)=\pi RD(1-H)c_V(0.27\alpha^2+1.30)$, where m is the mass of the droplet, R is the pinned contact-line radius, D is the water vapor diffusivity, c_v is the saturated water vapor concentration, H is the relative humidity, and α is the initial contact angle. For the calculation of the theoretical curves, we used the physical constants' values exposed in Table 1.

As shown in the Supplementary Information, the initial apex height h_0 and the time t_{eva} until the solvent is completely evapo-

Table 1
Physical constants of the suspensions used in this work.

Particle density, ρ (g/cm^3)	PS = 1.05; SiO_2 = 1.85
Particle radius, R_P (μm)	PS = 1.60; SiO_2 = 1.48
Particle concentration,c(mg/mL)	c(PS) = c(SiO_2) = 10
Solvent density, ρ (g/cm^3)	Water = 0.998
Dynamic viscosity,η (Pa.s)	1.003×10^{-3}
Initial contact angle, α (rad)	PS = 1.46 (84°); SiO_2 = 1.51 (87°)
Relative humidity, H (%)	27
Saturated water vapor concentration, c_v (g/cm^3)	2.320×10^{-5}
Water vapor diffusivity, D (m^2/s)	2.610×10^{-5}

rated out of the droplet can also be determined analytically. Whilst h_0 depends only on the droplet pinned contact radius and the initial contact angle, t_{eva} is further defined by two functions, namely $\beta(\alpha)$ and $f(\alpha)$. The determination of $\beta(\alpha)$ resembles the analytical solution introduced by Hu and Larson [41] (Eq. (3)), whereas $f(\alpha)$ is related to both $\beta(\alpha)$ and the contact angle α according to

$$\beta(\alpha) = -\frac{2}{\rho} D(1-H) c_V (0.27\alpha^2 + 1.30) \tag{3}$$

$$f(\alpha) = -\frac{(1-\cos(\alpha))^3}{3\beta(\alpha)\sin^3(\alpha)} - \frac{(1-\cos(\alpha))}{\beta(\alpha)\sin(\alpha)} \tag{4}$$

Taking into account Eqs. (2) to (4), we introduce the average interface velocity of the droplet apex u_i as

$$u_i(R,\alpha) = \frac{h_0(R,\alpha)}{R^2 f(\alpha)} = \frac{1}{R} g(\alpha) \tag{5}$$

where $g(\alpha) = (1-\cos(\alpha))/(\sin(\alpha) f(\alpha))$, which confirms that the interface velocity is inversely proportional to the droplet base radius ($u_i \propto 1/R$) [36,41] for pinned contact lines. It can be seen that the experimental and theoretical curves fit very well (Fig. 4 and Figure S3), which confirms the sophisticated evaporation analysis introduced by Hu and Larson. A simplified model for the average interface velocity has been introduced by Li *et al.* [32] in 2016 and described by $u_i = h_0/t_{eva}$. This model represented by the green dotted curve in Fig. 4, however, does not consider the contact angle or droplet radius, and does not fit the experimental measurements for the smallest droplets.

Fig. 4a demonstrates the non-linear reduction of the interface velocity with increasing droplet size. Here, the interface velocity is compared to the sedimentation u_s and the average capillary flow u_c calculated according to the Stokes' law (Eq. (1)) and (Eq. (6)), respectively.

$$u_c(R) = -\frac{3\beta(\alpha = \frac{\pi}{2})}{32R} \tag{6}$$

where u_c is the initial capillary flow averaged over the droplet base radius (See Supplementary Information for more details about the derivation based on the analytical solution by Hu and Larson [42]). Here it is important to note, that the capillary velocity does not represent a velocity component of the particle motion directly, but the flow velocity of the solvent. However, previous experimental results have proven the impact of the evaporation driven flow on the formation of a coffee ring [22] and the flow stays rather constant until the very last step of the droplet evaporation [43]. Moreover, the relative differences of u_c with droplet size remain constant over time (See Supplementary Information, Fig. 1). Thus, we use the initial capillary flow velocity as a representative value for u_c. The diffusion by Brownian or thermal motion is not included in our calculations, as we investigate micron-sized particles (3.2 μm of diameter), for which the gravitational Peclet number is way higher than the critical value (see Supplementary Information for details).

As it would be expected, the sedimentation speed is not altered by the droplet volume, whilst both the capillary and interface velocity are inversely proportional to the droplet base radius. For the measured contact angle of the PS particles $\alpha = 84^\circ$ we get a calculated value of $1.31 \times 10^3 \mu m^2/s$ for $g(\alpha)$, while the experimental data fit accounts $1.23 \times 10^3 \mu m^2/s$. For all droplet sizes, the interface velocity is higher than the capillary velocity. Moreover, our experimental results demonstrate a reduction of the CRE as well as the IE when the initial droplet volume is reduced. Therefore, in our experiments, particles must be inhibited from migration to the droplet periphery in smaller droplets. We associate this behavior to a "surface capturing effect", previously reported in other systems by different research groups [30,32]. Such effect causes the particles to accumulate at the receding droplet surface, due to a fast shrinkage of the liquid–air interface, thus capturing particles that were evenly distributed in the droplet (Fig. 4b). The capillary flow as well as sedimentation are still present, but the fast-receding droplet surface pushes the particles to the substrate, thereby preventing the migration to the droplet brim as well as drifting due to sedimentation on inclined surfaces. Noteworthy, previous studies initiated the surface capturing effect by heating of the substrate [30,32]. Here, for the first time we demonstrate that the reduction of the initial droplet volume causes the same effect, but only if the contact line stays pinned during evaporation.

To estimate a critical droplet size for the surface capturing effect to be fast enough to avoid a CRE, we proceed as follows. First, we define a critical length l_c that a particle should not exceed by migration during evaporation. For the homogenously dispersed particles in our system, we assume l_c to be equal to the average distance between particles in the initial droplet volume, which gives

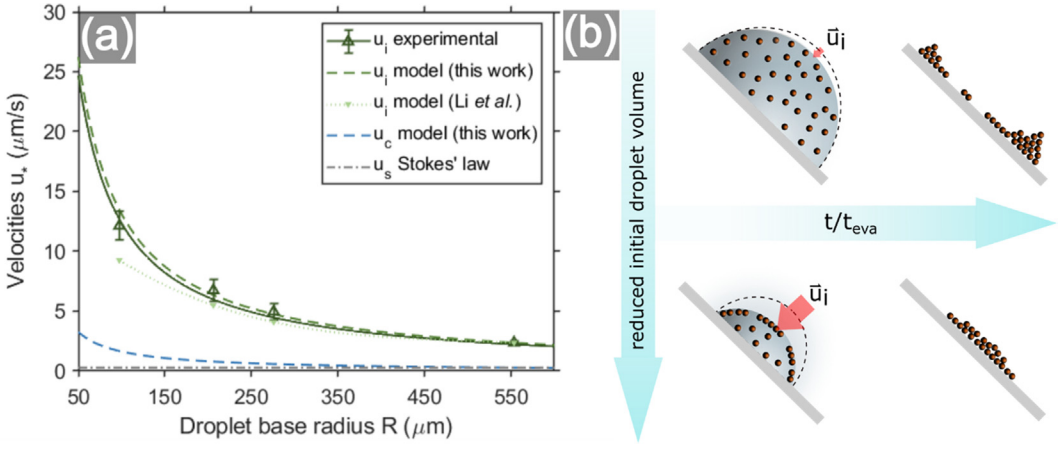

Fig. 4. (a) Effect of the reduction of the initial droplet volume/base radius on the three main driving velocities for particle deposition in evaporating PS droplets: data points of "u_i experimental" display the average liquid–air interface velocity and the solid line shows a fit of the model of this work (equation (5)) for the data points. "u_i model (this work)" presents the curve calculated by the aforementioned model and the constants from Table 1. "u_i model (Li *et al.*)" depicts the interface velocity calculated by Li's model. u_c is the averaged capillary flow for t = 0 (equation (6)), and u_s is the sedimentation velocity calculated by Stokes' law. The error bars for the interface velocity u_i represent the standard error for 10 replicates (b) Schematic illustration of the drying mechanisms for PS-suspensions: Upper scheme represents evaporation of "large" droplets, lower scheme presents particle deposition for "small" droplets. Each two snapshots on top of each other indicate the drying mechanism at the same point in time t/t_{eva}.

$l_c = R_P \sqrt[3]{4\pi\rho_P/3c}$ where R_P is the particle radius, ρ_P the particle density and c the concentration of the particles. With the values given in Table 1, the average distance for PS particles is l_c = 12 μm. Within the evaporation time t_{eva} the particles should not move by capillary flow or sedimentation parallel to the substrate more than l_c. Consequently $l_c \geq \min(u_c t_{eva}, \sin(\theta) u_s t_{eva})$. Putting these two equations together and introducing Eqs. (2) to (5) finally results in a formula for the calculation of the critical initial droplet radius R_c

$$R_c(\alpha, c, R_P) = \min\left(8l_c, \frac{1}{R_P}\sqrt{\frac{9l_c(c,R_P)\eta}{2\Delta\rho g \sin(\theta) f(\alpha)}}\right) \quad (7)$$

Here, the minimum function returns the smaller of the two radii. Introducing the values given in Table 1 we get for a tilted substrate with $\theta = 45^\circ$, $R_c(\mathrm{PS}) = \min(96\mu m, 248\mu m)$. Hence, for PS particles the capillary flow controls the CRE and, the resulting critical base radius accounts for R_c = 96 μm, which is very close to the base radius $R_{4.2nL}$ = 96.6 μm measured in the experiments. As this is a simple estimate of the critical droplet radius, this approach gives a good estimate of the critical droplet radius for a CRE-free printing of colloidal particles by direct writing.

As we confirmed the validity of Eqs. (2) and (7) for droplets with PS particles, we use the derived model to predict the critical droplet radii for different PS particle sizes, concentrations and relative humidity (Fig. 5a-c). The relation between the critical droplet radius and particle size is linear, while it decreases with increasing particle concentration, where it seems to reach a plateau for highly-loaded suspensions (>75 mg/mL). This indicates that the printing of homogeneous deposits shall be facilitated for colloidal suspensions with smaller concentration (<10 mg/mL) and bigger particles' size. Nonetheless, the synergetic effect between concentration and particle size on the critical radius should be taken into account, as it is more relevant for smaller concentrations, i.e. the decrease in moduli of the critical radius as the particle size decreases is bigger for smaller concentrations than higher concentrations. Note, we only consider particles with diameters between 1 and 4 μm, as thermal diffusion and sedimentation, respectively, may become relevant for particle sizes out of this range. Moreover, the nozzle size might have to be adjusted for bigger particles, whilst in this work we used the smallest possible needle size (34 Ga) available for the type of syringes used in our machine. For PS particles the humidity does not affect the critical radius in our model, because the critical radius depends on the capillary flow $u_c \propto (1-H)$ and $t_{eva} \propto 1/(1-H)$. Here it is important to note that u_c is the flow velocity of the solvent but not the particle velocity. For polymer particles of higher density, e.g. melamine (MF, $\rho_{MF} = 1.51 \frac{g}{cm^3}$), the critical droplet radius is limited due to sedimentation of the particles. In this case, printing of homogeneous structures is facilitated for lower humidity, since the evaporation time decreases, which reduces particle drift. Summarizing, to print homogeneous structures based on PS colloidal suspensions by direct writing one has to focus on smaller droplet sizes (line widths), smaller suspension concentration, and bigger particle sizes. The latter directly influences the properties of photonic crystals and glasses, so for our target application, it can't be varied, but might for other applications such as membranes, catalysts, filters, etc. If particles of higher density are printed, which limit the critical droplet size due to sedimentation primarily, humidity should be reduced to improve uniformity for droplets evaporating in stick mode.

Although the model is only compared to experimental data for PS particles, it may be applicable to other particles systems with similar surface charges, assuming a pinned contact line, which was not the case for SiO_2 particles, discussed in the next section.

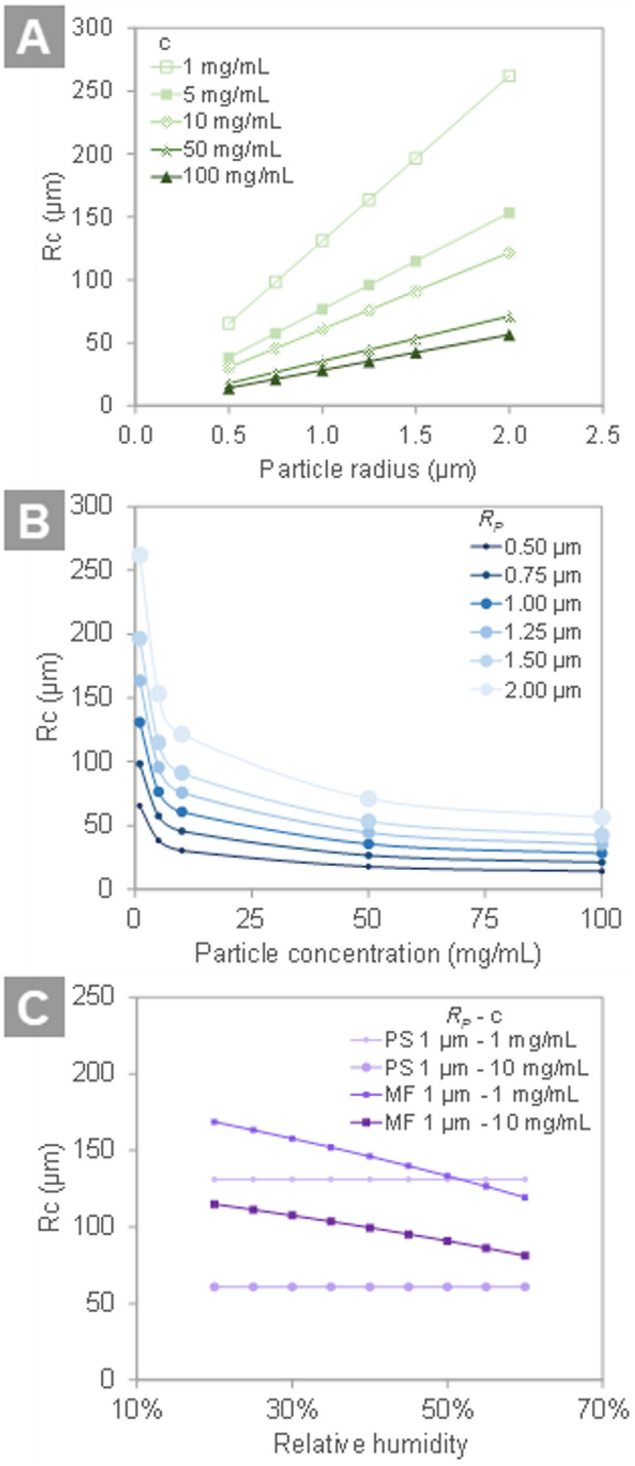

Fig. 5. Critical droplet radius for printing of PS colloidal suspensions as a function of (a) particle radius, (b) particle concentration and (c) relative humidity, according to different experimental conditions, namely, particle radius, and suspension concentration. The data points were generated according to the values predicted by the model described in this work (see text). A relative humidity of 27% is considered for the graphs (a and b), whereas an initial contact angle of 84° is used for (a-c). In (c) the critical base radius for suspensions containing MF-particles is additionally shown, to demonstrate exemplarily the influence of humidity for sedimentation limited particles' systems.

3.3.2. Silica suspension

Whereas droplets containing PS microparticles evaporated solely in stick mode, droplets of SiO_2 suspension began to continuously slip at a certain time point, depending on the droplet size.

The initial slip caused a temporary increase in droplet height and contact angle as well as a sudden decrease of the base radius which was resolved in the respective evolution curves (Fig. 6a, c) extracted from the *in-situ* monitoring of the evaporating droplets. This initial slip separates the overall evaporation into two phases, i.e. stick-mode phase and slip-mode phase. For the first time interval, i.e. with a pinned contact line, the mathematical model applied for PS holds true, thus the three velocity components where computed also for SiO_2, but solely considering the stick phase of each evaporation process. The interface velocity u_i and the initial capillary flow velocity u_c accelerated for smaller droplet volumes similar to previous findings for the PS suspension (Fig. 6b). Due to a higher density of the ceramic particles ($\rho_{SiO_2} = 1.85$ g/cm^3), however, the sedimentation velocity u_s as well as its tangential component u_{st} (for a 45° inclined surface) were faster than the capillary flow for all four investigated drop sizes and about as fast as the interface velocity for the largest droplet volume ($V_d = 208.7$ nL, $R = 549\mu m$). A surface capturing effect is impeded on an inclined surface, when the sedimentation component u_{sn} that is directed normal to the substrate, is faster or equal to the receding droplet surface, since particles cannot be captured by the receding droplet interface. For the largest droplet volume this coincides with the experimental results observed at the SEM and profilometry analyses (Fig. 3e, f) as particles assembled at the lower contact line due to particle drift, which is caused by sedimentation. However, even for smaller droplet sizes a surface capturing effect most likely did not primarily improve uniformity, since the deposits' shape changed from a kidney to a circular shape and formed domes instead of flat deposit (compare SiO_2 and PS deposits in Fig. 3d, h) although the same solid concentration was used for both suspensions. Instead, the slip mode might have improved uniformity, as demonstrated in a previous work by Xia *et al.* [46].

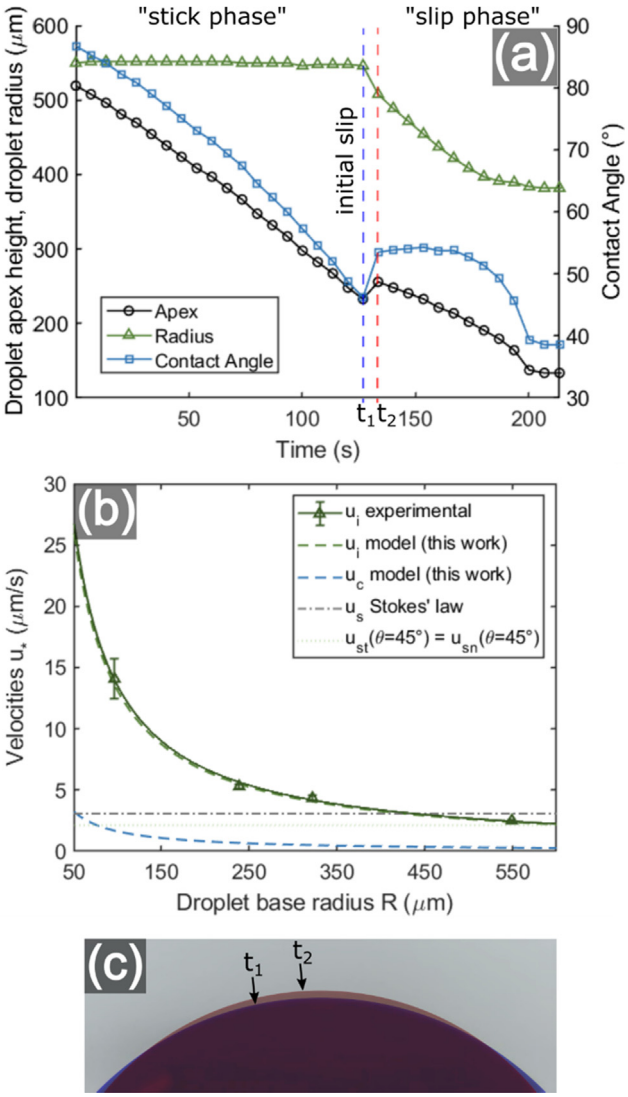

Fig. 6. (a) Apex height, base radius and contact angle evolution during droplet evaporation for SiO_2 suspension (208.7 nL, Θ = 0°). Vertical dashed blue (=t_1) and red line (=t_2) mark the point in evaporation time of the first contact line slip. This initial slip separates the droplet evaporation in two phases: "stick" phase and "slip" phase. (b) Graph depicts three main velocity components for single particles in evaporating droplets of different initial volume and base radius (only considering "stick" phase). Here, data points of "u_i experimental" display the average liquid–air interface velocity and the solid line shows a fit of the model of this work (Eq. (5)) for the data points. "u_i model (this work)" presents the curve calculated by the aforementioned model using the constants from Table 1. u_c is the averaged capillary flow for t = 0 (Eq. (6)), and u_s is the sedimentation velocity calculated by Stokes' law. Additionally, u_{st} and u_{sn} represent the tangential and normal component of u_s at a 45° inclined surface. The error bars for the interface velocity represent the standard error for 10 replicates. (c) Overlay of two snapshots for the evaporating droplet in (a). Blue colored snapshot visualizes drop profile at time t_1, the red droplet profile was acquired at time t_2. (For interpretation of the references to colour in this figure legend, the reader is referred to the web version of this article.)

The contact line of a droplet starts to slip as soon as a force comprised by the interfacial tensions of the three present phases (denoted as Young force [47]) overcomes the pinning force of the contact line [48]. The latter depends on surface roughness and chemical heterogeneities. The opposing Young force, however, depends on the contact angle and increases with a receding contact angle [47]. Therefore, the SiO_2 containing droplets eventually slip upon reaching a critical contact angle (α = 46° for 208.7 nL, Fig. 6a). Representative drop height evolution curves for each droplet volume are depicted in Fig. 7a. The black circular marker in each graph highlights the time point when the first slip event occurs. Apparently, the smaller the initial droplet volume was, the sooner the slip phase began, thus the more dominant the slip phase was. Additionally, an average time ratio t_s/t_{eva} was calculated for ten replicates of each droplet volume. Here, t_s is the time interval from the beginning of the droplet evaporation until the time point of the initial slip. The smaller the ratio, the more dominant was the slip phase. For all four volumes under consideration, i.e. 208.7 nL, 41.7 nL, 20.9 nL and 4.2 nL, the average time ratios were 0.58, 0.57, 0.48 and 0.40, respectively, with a maximum standard error of 0.08. These ratios coincide with an accelerated interface velocity. The smaller the droplet volume, the faster the interface recedes, hence the sooner the critical contact angle is reached, and the slipping of the contact line is induced. Due to the receding contact line in the slip phase, less solvent must be replenished at the droplet rim, thereby the capillary flow gets reduced. Hence, a slip dominated evaporation, i.e. obtained here with smaller initial droplet volume, lowers the coffee ring effect for SiO_2 particles. These results are in agreement with previous results regarding self-assembly onto superhydrophobic surfaces [46], in which also the slip-mode evaporation is promoted and thereby, the homogeneity of the deposits increased.

Additionally, a receding contact line confines the particle assembly spatially, which therefore can also reduce the theoretical drift due to inclination. Consequently, lowering the initial droplet volume, which promotes a slip dominated evaporation, reduces the IE (See Fig. 3e-h and Fig. 7b), thus forming more uniform dome-shaped depositions on inclined surfaces due to a "confinement effect", even though the substrate being used in this work is not superhydrophobic.

We demonstrate for the first time that both the CRE and IE can be completely suppressed by simply reducing the dispense volume

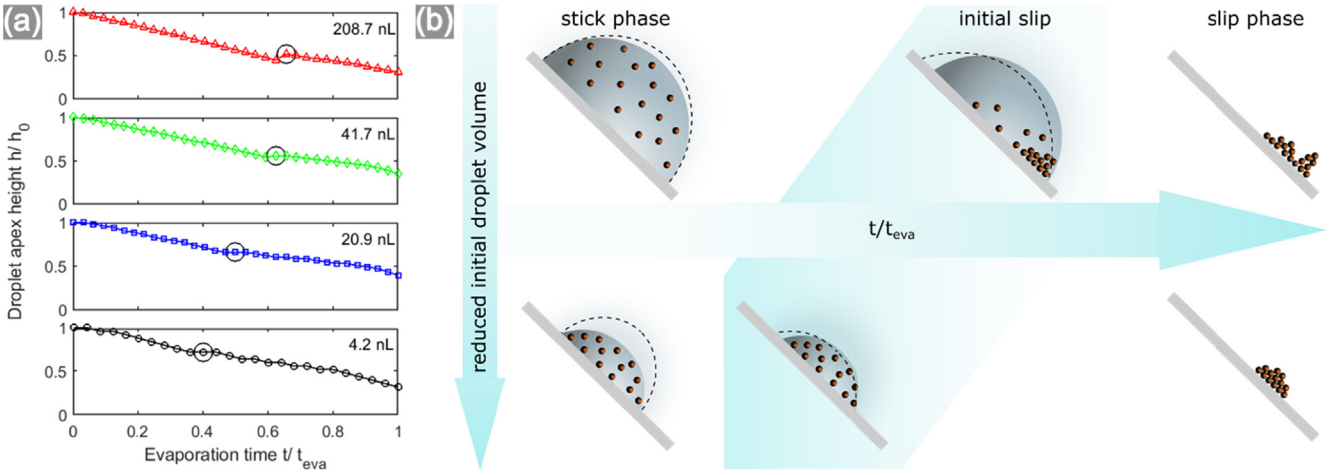

Fig. 7. (a) Droplet apex height reduction during evaporation of SiO_2-suspensions for different initial droplet volumes of 208.7 nL, 41.7 nL, 20.9 nL and 4.2 nL. Black circular markers highlight the slip event (change from stick to slip mode). (b) Schematic drawing of the drying mechanism and particle deposition for SiO_2 suspension on aluminum oxide substrate. Upper and lower cross sections are representative for "large" and "small" initial droplet volume, respectively. The lateral position in reference to the arrow for time t/t_{eva} illustrates the point in evaporation time. Cross sections during the initial slip for both droplet volumes are highlighted by a blue background that separates stick- and slip modes. (For interpretation of the references to colour in this figure legend, the reader is referred to the web version of this article.)

during automated printing of PS and SiO_2 colloidal suspensions by direct writing. The dispense volume reduction enhances the surface capturing effect for stick mode evaporation, and further confinement effect for mixed stick–slip mode evaporation, forming uniform particle deposits. A comparison of our results with that of previous studies and their respective approaches to reduce the coffee ring effect and also the inclination effect is available in Table S1. The reduction of the droplet size as a mean to reduce CRE has also been demonstrated by Shen *et al.* [44], however only for nanoparticles deposited on horizontally aligned substrates, which requires considering different particle motion components than in our work with micron-sized particles, e.g. particle diffusion instead of sedimentation. Regarding the IE effect, there are very few studies covering self-assembly on inclined surfaces. Nonetheless, the recent work by Gopu *et al.* [36] agrees with the results obtained in this work, as they also observed a reduction in the IE of droplets deposited on vertical substrates by electrospraying, but, different from this work, they were not able to avoid or reduce the CRE. Note, we exclude here studies on vertical convective self-assembly, as structures produced by such are known to have significant height profile variations [49,50], and also assembly processes for monolayers such as Langmuir-Blodgett or floating assembly. Several other approaches [23] to form homogeneous particle deposits have been studied over the past years (Table S1). However, exploiting particle shape [51] or size [28], adding surfactants [52], adjusting pH [29] or particle-interface interactions [31], and using hydrophobic substrates [53] restricts the applicability of each approach to certain materials and chemical compounds. Moreover, depending on the application, specific particle sizes or substrates are needed and cannot be modified. For our application example - reflective thermal barrier coatings - it is necessary to produce the colloidal templates with particles of about 3 μm in diameter, so the reflection is maximized in the infrared range [4].

4. Conclusion

It was shown that reducing the dispense volume during printing of colloidal suspensions by direct writing is a facile but versatile and powerful approach to enable homogeneous coating of inclined surfaces with colloidal-based structures. The inclination of the substrate causes microparticles to drift during colloidal assembly resulting in an anisotropic deposition, which is counterbalanced by the surface capturing effect and confinement effect, enhanced when the dispense volume is reduced. We introduced a critical base radius R_c that gives an estimate for the minimum droplet size to print homogenous deposits on inclined surfaces with microparticles' suspensions evaporating in stick mode. Furthermore, we demonstrated that our approach also works for droplets evaporating in stick–slip mode.

We used the direct writing technique to deposit single droplets on inclined surfaces in a very precise and automated way. This printing process can be expanded for printing lines [21] and upon development of the additive manufacturing of lines, whole areas on even or complex 3D surfaces in an automated way. A variety of coating techniques have already been studied and are frequently used to form particulate layers from monodisperse particles such as drop casting [35,36,45,54], vertical convective self-assembly [51,50,55], spin coating [56,57], or angle controlled inclined deposition [58]. However, none of these techniques can be used to coat inclined surfaces homogenously with localized high-precision coatings in an automated way. This is possible by direct writing combined with colloidal assembly. In this sense, the reduction of the dispense volume is a versatile and promising approach to produce homogeneous structures. The printing of lines has already been demonstrated for this process [21], with pronounced CRE, though. To print homogeneous lines, it is necessary to adjust the direct writing dispense rate to the particles' self-assembly rate, and knowledge about the evaporation mode and critical radius is essential to accomplish this. Future studies on the AMCA process or related additive manufacturing processes can thus profit from the approach demonstrated in our study and the corresponding developed model to improve printing in higher dimensions, i.e. printing lines and layers.

CRediT authorship contribution statement

Benedikt F. Winhard: Investigation, Data curation, Validation, Formal analysis, Writing - original draft, Visualization. **Stefanie Haugg:** Investigation, Writing - review & editing. **Robert Blick:** Resources, Funding acquisition, Supervision. **Gerold A. Schneider:** Methodology, Visualization, Writing - review & editing, Resources, Funding acquisition, Project administration, Supervision. **Kaline P. Furlan:** Conceptualization, Methodology, Visualization, Writing -

review & editing, Funding acquisition, Project administration, Supervision.

Declaration of Competing Interest

The authors declare that they have no known competing financial interests or personal relationships that could have appeared to influence the work reported in this paper.

Acknowledgments

The authors gratefully acknowledge the financial support from the Deutsche Forschungsgemeinschaft (DFG, German Research Foundation) – Projektnummer 192346071 – SFB 986, project C4. Dr. Kaline P. Furlan also gratefully acknowledge Balten Lauströer and Manfred Geerken for their support on setting up the AMCA equipment at TUHH, Dr. Berta Domènech for the scientific discussions regarding the AMCA of different colloidal systems, Dr. Robert Zierold for proofreading and Prof. Patrick Huber for the scientific discussion and valuable input regarding the contact angle measurements.

Appendix A. Supplementary material

Supplementary data to this article can be found online at https://doi.org/10.1016/j.jcis.2021.03.017.

References

[1] M. Karg, T.A.F. König, M. Retsch, C. Stelling, P.M. Reichstein, T. Honold, M. Thelakkat, A. Fery, Colloidal self-assembly concepts for light management in photovoltaics, Mater. Today 18 (4) (2015) 185–205, https://doi.org/10.1016/j.mattod.2014.10.036.
[2] G. Shang, P. Dyachenko, E.W. Leib, T. Vossmeyer, A. Petrov, M. Eich, Conductive and radiative heat transfer inhibition in YSZ photonic glass, Ceram. Int. 46 (11) (2020) 19241–19247, https://doi.org/10.1016/j.ceramint.2020.04.262.
[3] H.S. Lee, R. Kubrin, R. Zierold, A.Y. Petrov, K. Nielsch, G.A. Schneider, M. Eich, Thermal radiation transmission and reflection properties of ceramic 3D photonic crystals, J. Opt. Soc. Am. B 29 (3) (2012) 450, https://doi.org/10.1364/JOSAB.29.000450.
[4] J.J. do Rosário, Y. Häntsch, R.M. Pasquarelli, P.N. Dyachenko, E. Vriend, A.Y. Petrov, K.P. Furlan, M. Eich, G.A. Schneider, Advancing the fabrication of YSZ-inverse photonic glasses for broadband omnidirectional reflector films, J. Eur. Ceram. Soc. 39 (11) (2019) 3353–3363, https://doi.org/10.1016/j.jeurceramsoc.2019.04.028.
[5] K.P. Furlan, E. Larsson, A. Diaz, M. Holler, T. Krekeler, M. Ritter, A.Y. Petrov, M. Eich, R. Blick, G.A. Schneider, I. Greving, R. Zierold, R. Janßen, Photonic materials for high-temperature applications: Synthesis and characterization by X-ray ptychographic tomography, Appl. Mater. Today 13 (2018) 359–369, https://doi.org/10.1016/j.apmt.2018.10.002.
[6] P. Bueno, K. Pagnan Furlan, D. Hotza, R. Janssen, High-temperature stable inverse opal photonic crystals via mullite-sol-gel infiltration of direct photonic crystals, J Am Ceram Soc 24 (5) (2018) 13146, https://doi.org/10.1111/jace.16012.
[7] R.M. Pasquarelli, H.S. Lee, R. Kubrin, R. Zierold, A.Y. Petrov, K. Nielsch, G.A. Schneider, M. Eich, R. Janssen, Enhanced structural and phase stability of titania inverse opals, J. Eur. Ceram. Soc. 35 (11) (2015) 3103–3109, https://doi.org/10.1016/j.jeurceramsoc.2015.04.041.
[8] P.N. Dyachenko, J.J. do Rosário, E.W. Leib, A.Y. Petrov, M. Störmer, H. Weller, T. Vossmeyer, G.A. Schneider, M. Eich, Tungsten band edge absorber/emitter based on a monolayer of ceramic microspheres, Optics express 2015, 23 (19), A1236–A1244. http://doi.org/10.1364/OE.23.0A1236.
[9] P.N. Dyachenko, J.J. do Rosário, E.W. Leib, A.Y. Petrov, R. Kubrin, G.A. Schneider, H. Weller, T. Vossmeyer, M. Eich, Ceramic Photonic Glass for Broadband Omnidirectional Reflection, ACS Photon. 2014, 1 (11), 1127–1133. http://doi.org/10.1021/ph500224r.
[10] M. Finsel, M. Hemme, S. Döring, J.S.V. Rüter, G.T. Dahl, T. Krekeler, A. Kornowski, M. Ritter, H. Weller, T. Vossmeyer, Synthesis and thermal stability of ZrO 2 @SiO 2 core–shell submicron particles, RSC Adv. 9 (46) (2019) 26902–26914, https://doi.org/10.1039/C9RA05078G.
[11] E.W. Leib, R.M. Pasquarelli, M. Blankenburg, M. Müller, A. Schreyer, R. Janssen, H. Weller, T. Vossmeyer, High-Temperature Stable Zirconia Particles Doped with Yttrium, Lanthanum, and Gadolinium, Part. Part. Syst. Charact. 33 (9) (2016) 645–655, https://doi.org/10.1002/ppsc.201600069.
[12] E.W. Leib, R.M. Pasquarelli, J.J. do Rosário, P.N. Dyachenko, S. Döring, A. Puchert, A.Y. Petrov, M. Eich, G.A. Schneider, R. Janssen, H. Weller, T. Vossmeyer, Yttria-stabilized zirconia microspheres: novel building blocks for high-temperature photonics, J. Mater. Chem. C 4 (1) (2016) 62–74, https://doi.org/10.1039/C5TC03260A.
[13] E.W. Leib, U. Vainio, R.M. Pasquarelli, J. Kus, C. Czaschke, N. Walter, R. Janssen, M. Müller, A. Schreyer, H. Weller, T. Vossmeyer, Synthesis and thermal stability of zirconia and yttria-stabilized zirconia microspheres, J. Colloid Interface Sci. 448 (2015) 582–592, https://doi.org/10.1016/j.jcis.2015.02.049.
[14] N. Nafsin, H. Li, E.W. Leib, T. Vossmeyer, P. Stroeve, R.H.R. Castro, Stability of rare-earth-doped spherical yttria-stabilized zirconia synthesized by ultrasonic spray pyrolysis, J Am Ceram Soc 100 (10) (2017) 4425–4434, https://doi.org/10.1111/jace.14971.
[15] M. Ogurreck, J.J. do Rosario, E.W. Leib, D. Laipple, I. Greving, F. Marschall, A. Last, G.A. Schneider, T. Vossmeyer, H. Weller, F. Beckmann, M. Müller, Determination of the packing fraction in photonic glass using synchrotron radiation nanotomography, J. Synchrotron Radiation 23 (Pt 6) (2016) 1440–1446, https://doi.org/10.1107/S1600577516012960.
[16] M. Knez, K. Nielsch, L. Niinistö, Synthesis and Surface Engineering of Complex Nanostructures by Atomic Layer Deposition, Adv. Mater. 19 (21) (2007) 3425–3438, https://doi.org/10.1002/adma.200700079.
[17] K.P. Furlan, T. Krekeler, M. Ritter, R. Blick, G.A. Schneider, K. Nielsch, R. Zierold, R. Janßen, Low-Temperature Mullite Formation in Ternary Oxide Coatings Deposited by ALD for High-Temperature Applications, Adv. Mater. Interfaces 4 (23) (2017) 1700912, https://doi.org/10.1002/admi.201700912.
[18] N. Vogel, M. Retsch, C.-A. Fustin, A. Del Campo, U. Jonas, Advances in colloidal assembly: the design of structure and hierarchy in two and three dimensions, Chem. Rev. 115 (13) (2015) 6265–6311, https://doi.org/10.1021/cr400081d.
[19] H.G. Campos, K.P. Furlan, D.E. Garcia, R. Blick, R. Zierold, M. Eich, D. Hotza, R. Janssen, Effects of processing parameters on 3D structural ordering and optical properties of inverse opal photonic crystals produced by atomic layer deposition, Int. Jnl. Ceramic Engine Sci. 1 (2) (2019) 68–76, https://doi.org/10.1002/ces2.10015.
[20] W. Ai-Jun, C. Sheng-Li, D. Peng, C. Xiao-Gang, Z. Qian, Y. Gui-Mei, H. Chun-Tian, Z. Dao-Zhong, Fabrication of Colloidal Photonic Crystals with Heterostructure by Spin-Coating Method, Chin. Phys. Lett., 26 (2), 24210. 10.1088/0256-307X/26/2/024210.
[21] A.T.L. Tan, S. Nagelberg, E. Chang-Davidson, J. Tan, J.K.W. Yang, M. Kolle, A.J. Hart, In-Plane Direct-Write Assembly of Iridescent Colloidal Crystals, Small 16 (4) (2020), https://doi.org/10.1002/smll.201905519 e1905519.
[22] R.D. Deegan, O. Bakajin, T.F. Dupont, G. Huber, S.R. Nagel, T.A. Witten, Capillary flow as the cause of ring stains from dried liquid drops, Nature 389 (6653) (1997) 827–829, https://doi.org/10.1038/39827.
[23] D. Mampallil, H.B. Eral, A review on suppression and utilization of the coffee-ring effect, Adv. Colloid Interface Sci. 252 (2018) 38–54, https://doi.org/10.1016/j.cis.2017.12.008.
[24] X. Man, M. Doi, Ring to Mountain Transition in Deposition Pattern of Drying Droplets, Phys. Rev. Lett. 116 (6) (2016) 66101, https://doi.org/10.1103/PhysRevLett.116.066101.
[25] J. Freed-Brown, Evaporative deposition in receding drops, Soft Matter 10 (47) (2014) 9506–9510, https://doi.org/10.1039/c4sm02133a.
[26] M. Dicuangco, S. Dash, J.A. Weibel, S.V. Garimella, Effect of superhydrophobic surface morphology on evaporative deposition patterns, Appl. Phys. Lett. 104 (20) (2014), https://doi.org/10.1063/1.4878322 201604.
[27] H. Hu, R.G. Larson, Marangoni effect reverses coffee-ring depositions, J. Phys. Chem. B 110 (14) (2006) 7090–7094, https://doi.org/10.1021/jp0609232.
[28] W. Li, W. Ji, H. Sun, D. Lan, Y. Wang, Pattern Formation in Drying Sessile and Pendant Droplet: Interactions of Gravity Settling, Interface Shrinkage, and Capillary Flow, Langmuir: ACS J. Surf. Colloids 35 (1) (2019) 113–119, https://doi.org/10.1021/acs.langmuir.8b02659.
[29] R. Bhardwaj, X. Fang, P. Somasundaran, D. Attinger, Self-assembly of colloidal particles from evaporating droplets: role of DLVO interactions and proposition of a phase diagram, Langmuir: ACS J. Surf. Colloids 26 (11) (2010) 7833–7842, https://doi.org/10.1021/la9047227.
[30] T.A.H. Nguyen, S.R. Biggs, A.V. Nguyen, Manipulating colloidal residue deposit from drying droplets: Air/liquid interface capture competes with coffee-ring effect, Chem. Eng. Sci. 167 (2017) 78–87, https://doi.org/10.1016/j.ces.2017.04.001.
[31] T.P. Bigioni, X.-M. Lin, T.T. Nguyen, E.I. Corwin, T.A. Witten, H.M. Jaeger, Kinetically driven self assembly of highly ordered nanoparticle monolayers, Nat. Mater. 5 (4) (2006) 265–270, https://doi.org/10.1038/nmat1611.
[32] Y. Li, Q. Yang, M. Li, Y. Song, Rate-dependent interface capture beyond the coffee-ring effect, Sci. Rep. 6 (2016) 24628, https://doi.org/10.1038/srep24628.
[33] J.R. Trantum, Z.E. Eagleton, C.A. Patil, J.M. Tucker-Schwartz, M.L. Baglia, M.C. Skala, F.R. Haselton, Cross-sectional tracking of particle motion in evaporating drops: flow fields and interfacial accumulation, Langmuir: ACS J. Surf. Colloids 29 (21) (2013) 6221–6231, https://doi.org/10.1021/la400542x.
[34] K.N. Al-Milaji, H. Zhao, New Perspective of Mitigating the Coffee-Ring Effect: Interfacial Assembly, J. Phys. Chem. C 123 (19) (2019) 12029–12041, https://doi.org/10.1021/acs.jpcc.9b00797.
[35] X. Du, R.D. Deegan, Ring formation on an inclined surface, J. Fluid Mech. 775 (2015), https://doi.org/10.1017/jfm.2015.312.
[36] M. Gopu, S. Rathod, U. Namangalam, R.K. Pujala, S.S. Kumar, D. Mampallil, Evaporation of Inclined Drops: Formation of Asymmetric Ring Patterns, Langmuir: ACS J. Surf. Colloids (2020), https://doi.org/10.1021/acs.langmuir.0c01084.
[37] T.-S. Wong, T.-H. Chen, X. Shen, C.-M. Ho, Nanochromatography driven by the coffee ring effect, Anal. Chem. 83 (6) (2011) 1871–1873, https://doi.org/10.1021/ac102963x.

[38] V.H. Chhasatia, Y. Sun, Interaction of bi-dispersed particles with contact line in an evaporating colloidal drop, Soft Matter 7 (21) (2011) 10135, https://doi.org/10.1039/c1sm06393f.
[39] P.-G. de Gennes, F. Brochard-Wyart, D. Quéré, Capillarity and Gravity. In Capillarity and wetting phenomena: Drops, bubbles, pearls, waves; Gennes, P.-G. de, Brochard-Wyart, F., Quéré, D., Eds.; Springer, 2010; pp. 33–67. http://doi.org/10.1007/978-0-387-21656-0_2.
[40] S. Wong, V. Kitaev, G.A. Ozin, Colloidal crystal films: advances in universality and perfection, J. Am. Chem. Soc. 125 (50) (2003) 15589–15598, https://doi.org/10.1021/ja0379969.
[41] H. Hu, R.G. Larson, Evaporation of a Sessile Droplet on a Substrate, J. Phys. Chem. B 106 (6) (2002) 1334–1344, https://doi.org/10.1021/jp0118322.
[42] H. Hu, R.G. Larson, Analysis of the microfluid flow in an evaporating sessile droplet, Langmuir: ACS J. Surf. Colloids 21 (9) (2005) 3963–3971, https://doi.org/10.1021/la047528s.
[43] Á.G. Marín, H. Gelderblom, D. Lohse, J.H. Snoeijer, Order-to-disorder transition in ring-shaped colloidal stains, Phys. Rev. Lett. 107 (8) (2011) 85502, https://doi.org/10.1103/PhysRevLett.107.085502.
[44] X. Shen, C.-M. Ho, T.-S. Wong, Minimal size of coffee ring structure, J. Phys. Chem. B 114 (16) (2010) 5269–5274, https://doi.org/10.1021/jp912190v.
[45] N.R. Devlin, K. Loehr, M.T. Harris, The importance of gravity in droplet evaporation: A comparison of pendant and sessile drop evaporation with particles, AIChE J. 62 (3) (2016) 947–955, https://doi.org/10.1002/aic.15120.
[46] T. Xia, W. Luo, F. Hu, W. Qiu, Z. Zhang, Y. Lin, X.Y. Liu, Fabrication of Crack-Free Photonic Crystal Films on Superhydrophobic Nanopin Surface, ACS Appl. Mater. Interfaces 9 (26) (2017) 22037–22041, https://doi.org/10.1021/acsami.7b04653.
[47] J.M. Stauber, S.K. Wilson, B.R. Duffy, K. Sefiane, On the lifetimes of evaporating droplets with related initial and receding contact angles, Phys. Fluids 27 (12) (2015), https://doi.org/10.1063/1.4935232 122101.
[48] A. Amini, G.M. Homsy, Evaporation of liquid droplets on solid substrates. I. Flat substrate with pinned or moving contact line, Phys. Rev. Fluids 2 (4) (2017) 43603, https://doi.org/10.1103/PhysRevFluids.2.043603.
[49] L. Cademartiri, A. Sutti, G. Calestani, C. Dionigi, P. Nozar, A. Migliori, Flux-Assisted Self-Assembly of Monodisperse Colloids, Langmuir 19 (19) (2003) 7944–7947, https://doi.org/10.1021/la034485r.
[50] H. Cong, W. Cao, Colloidal Crystallization Induced by Capillary Force, Langmuir 19 (20) (2003) 8177–8181, https://doi.org/10.1021/la0344480.
[51] P.J. Yunker, T. Still, M.A. Lohr, A.G. Yodh, Suppression of the coffee-ring effect by shape-dependent capillary interactions, Nature 476 (7360) (2011) 308–311, https://doi.org/10.1038/nature10344.
[52] T. Still, P.J. Yunker, A.G. Yodh, Surfactant-induced Marangoni eddies alter the coffee-rings of evaporating colloidal drops, Langmuir: ACS J. Surf. Colloids 28 (11) (2012) 4984–4988, https://doi.org/10.1021/la204928m.
[53] H.-Y. Ko, J. Park, H. Shin, J. Moon, Rapid Self-Assembly of Monodisperse Colloidal Spheres in an Ink-Jet Printed Droplet, Chem. Mater. 16 (22) (2004) 4212–4215, https://doi.org/10.1021/cm035256t.
[54] L. Bansal, P. Seth, S. Sahoo, R. Mukherjee, S. Basu, Beyond coffee ring: Anomalous self-assembly in evaporating nanofluid droplet on a sticky biomimetic substrate, Appl. Phys. Lett. 113 (21) (2018), https://doi.org/10.1063/1.5063605 213701.
[55] S. Matsushita, T. Takagi, K. Kamimura, T. Kasaya, H.T. Miyazaki, Enhanced light diffraction from self-assembled double-layer colloidal crystals, J. Appl. Phys. 110 (6) (2011) 63104, https://doi.org/10.1063/1.3636104.
[56] A. Mihi, M. Ocaña, H. Míguez, Oriented Colloidal-Crystal Thin Films by Spin-Coating Microspheres Dispersed in Volatile Media, Adv. Mater. 18 (17) (2006) 2244–2249, https://doi.org/10.1002/adma.200600555.
[57] P. Jiang, M.J. McFarland, Large-scale fabrication of wafer-size colloidal crystals, macroporous polymers and nanocomposites by spin-coating, J. Am. Chem. Soc. 126 (42) (2004) 13778–13786, https://doi.org/10.1021/ja0470923.
[58] Z.-F. Chen, Y.-Y. Xiong, P. Han, Y.-H. Chen, H. Xiao, A colloidal crystal double-heterostructure fabricated with the angle controlled inclined deposition method, Chin. Phys. B 21 (7) (2012) 78103, https://doi.org/10.1088/1674-1056/21/7/078103.